

# Free-Breathing Liver Fat, $R_2^*$ and $B_0$ Field Mapping Using Multi-Echo Radial FLASH and Regularized Model-based Reconstruction

Zhengguo Tan, Christina Unterberg-Buchwald, Moritz Blumenthal, Nick Scholand, Philip Schaten, Christian Holme, Xiaoqing Wang, Dirk Raddatz, Martin Uecker

**Abstract**—This work introduced a stack-of-radial multi-echo asymmetric-echo MRI sequence for free-breathing liver volumetric acquisition. Regularized model-based reconstruction was implemented in Berkeley Advanced Reconstruction Toolbox (BART) to jointly estimate all physical parameter maps (water, fat,  $R_2^*$ , and  $B_0$  field inhomogeneity maps) and coil sensitivity maps from self-gated  $k$ -space data. Specifically, locally low rank and temporal total variation constraints were employed directly on physical parameter maps. The proposed free-breathing radial technique was tested on a water/fat & iron phantom, a young volunteer, and obesity/diabetes/hepatitis steatosis patients. Quantitative fat fraction and  $R_2^*$  accuracy were confirmed by comparing our technique with the reference breath-hold Cartesian scan. The multi-echo radial sampling sequence achieves fast  $k$ -space coverage and is robust to motion. Moreover, the proposed motion-resolved model-based reconstruction allows for free-breathing liver fat and  $R_2^*$  quantification of multiple motion states. Overall, our proposed technique offers a convenient tool for non-invasive liver assessment with no breath holding requirement.

**Index Terms**—calibration-less compressed sensing parallel imaging, model-based reconstruction, multi-echo radial sampling,  $R_2^*$  mapping, water/fat separation.

## I. INTRODUCTION

Manuscript received xxx xx, xxxx; accepted xxx xx, xxxx. Date of publication xxx xx, xxxx. This work was supported by DFG (German Research Foundation) - TA 1473/2-1, UE 189/4-1, and EXC 2067/1-390729940, DZHK (German Centre for Cardiovascular Research) and NIH U24EB029240.

Z. T. was with Institute for Diagnostic and Interventional Radiology, University Medical Center Göttingen (UMG). He is now with Department of Artificial Intelligence in Biomedical Engineering, University of Erlangen-Nuremberg (e-mail: zhengguo.tan@fau.de).

C. U. is with Department of Cardiology and Pulmonology, UMG (e-mail: unterberg@med.uni-goettingen.de).

M. B., N. S., and P. S. are with Institute for Diagnostic and Interventional Radiology, UMG (e-mail: moritz.blumenthal@med.uni-goettingen.de; nick.scholand@med.uni-goettingen.de; philip.schaten@med.uni-goettingen.de).

C. H. and X. W. were with Institute for Diagnostic and Interventional Radiology, UMG. They are now with Institute of Biomedical Imaging, Graz University of Technology (e-mail: christian.holme@med.uni-goettingen.de; xiaoqing.wang@med.uni-goettingen.de).

D. R. is with Clinic of Gastroenterology, Gastrointestinal Oncology and Endocrinology, UMG (e-mail: draddatz@med.uni-goettingen.de).

M. U. is with Institute of Biomedical Imaging, Graz University of Technology and Institute for Diagnostic and Interventional Radiology, UMG (e-mail: uecker@tugraz.at).

QUANTITATIVE parameter mapping of the liver is of interest in basic research and clinical practice. Specifically, quantitative proton density fat fraction (PDFF) and  $R_2^*$  maps have been shown to be non-invasive imaging biomarkers for hepatic steatosis [1], [2] and iron overload [3], [4], respectively. Originating from the two-echo chemical-shift-encoded Dixon method [5] for qualitative water/fat separation, quantitative assessment of liver fat and iron decomposition firstly requires multi-echo chemical-shift encoding (e.g. low flip angle multi-gradient-echo acquisition). Conventional acquisition methods require subjects to perform proper breath hold. Therefore, incomplete breath hold or incompliant patients can induce pronounced image artifacts, thereby hampering the quantification of liver fat and  $R_2^*$ .

To address the respiratory motion problem, several recent works proposed free-breathing liver fat and  $R_2^*$  mapping. Armstrong et al. [6] and Zhong et al. [7], [8] proposed to use stack-of-radial multi-echo sampling with bipolar gradients. Sampled echoes were then binned into four respiratory phases and reconstructed via NUFFT [9]. Liver fat and  $R_2^*$  maps are quantified via physics modeling [10]–[12] and image-space fitting [13]–[15]. Schneider et al. [16] employed model-based reconstruction [17]–[19] to jointly reconstruct water, fat, and  $R_2^*$  maps directly from  $k$ -space data with spatial total variation (TV) regularization, whereas the  $B_0$  field inhomogeneity map was pre-calibrated [14] and kept constant. Wang et al. [20] implemented inversion recovery (IR) magnetization preparation before multi-echo readouts and applied the multi-tasking reconstruction technique [21] to reconstruct respiratory motion resolved multi-echo and IR images. Subsequently, these images were used for model fitting [14] to obtain quantitative fat,  $R_2^*$ , and water-specific  $T_1$  maps. Starekova et al. [22] proposed a 2D acquisition scheme with a non-local means [23] motion-corrected averaging technique.

Among these free-breathing techniques, only the work from Schneider et al. employed model-based reconstruction. However, this work did not allow for  $B_0$  update during motion-resolved model-based reconstruction. Joint  $B_0$  estimation is challenging. On the one hand,  $B_0$  fluctuations induced by respiratory motion result in temporarily varying  $B_0$  maps. On the other hand, the  $B_0$  field map term appears as a non-linear term in the water/fat separation problem. One popular proposal is to enforce spatial smoothness of the  $B_0$  field map via first-

R1.4

R1.3

R1.7

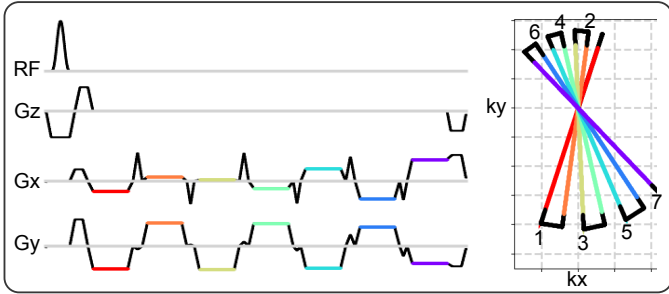


**Fig. 1.** (Left) One representative repetition time (TR) block of the proposed multi-echo asymmetric-echo radial sequence. (Right) The corresponding  $k$ -space trajectory. The echoes are color coded, indicating the period when ADC is switched on, while the dark solid lines indicate either the ramp or the blip gradients. The colored arrows near to echo numbers illustrate the readout direction.

R1.8 or second-order finite-difference regularization [24]–[26].  
R1.8 Although promising, it may still be challenging when phase wraps occur along echoes.

R2.13 The contribution of this work is two-fold. First, to achieve more efficient and faster acquisition, our work combined multi-echo asymmetric-echo radial fast low-angle shot (FLASH) with stack-of-stars volumetric acquisition [27] for free-breathing acquisition. Second, we implemented a regularized model-based reconstruction method for joint estimation of all quantitative parameter maps and coil sensitivity maps directly from  $k$ -space data. We solved the nonlinear inverse problem via iteratively regularized Gauss-Newton method (IRGNM) [28] with the alternating direction method of multipliers (ADMM), allowing for generalized regularization terms [29]. We validated the proposed acquisition and reconstruction methods by comparing with the reference breath-hold Cartesian scan [15] through patients diagnosed with obesity, diabetes, or non-alcoholic fatty liver disease (NAFLD). This work achieves joint estimation of water, fat,  $R_2^*$  and  $B_0$  maps for free-breathing volumetric liver quantification with reduced scan time.

## II. THEORY

### A. Multi-Echo Radial Sampling

Data acquisition is based on the multi-echo radial sampling sequence [30]. As depicted in Fig. 1, seven gradient echoes per RF excitation were acquired. All radial spokes within one frame were uniformly distributed in  $k$ -space and the angle increment between frames was the small Golden angle [31] ( $\approx 68.75^\circ$ ). The angles of the radial spokes within one frame are  $\theta_{l,m} = 2\pi \cdot [(l-1) \cdot N_{\text{echo}} + m - 1] / (N_{\text{echo}} \cdot N_{\text{shot}})$  with  $l$  and  $m$  being the excitation and echo index, respectively. To foster echo asymmetry and shorten scan time, asymmetric echoes (i.e. partial Fourier readouts) were employed in combination with multi-echo sampling.

### B. Nonlinear Signal Model

Parallel MRI [32]–[34] simultaneously receives signals from multiple receiver coils, and is extendable to include multiple echoes when using long echo-train MRI sequences,

$$y_{j,m}(t) = \int d\vec{r} e^{-i2\pi\vec{k}(t)\cdot\vec{r}} c_j(\vec{r}) \rho_m(\vec{r}), \quad (1)$$

with  $c_j$  and  $\rho_m$  being the  $j$ th coil sensitivity map and the  $m$ th echo image, respectively.  $y_{j,m}(t)$  is the acquired multi-coil multi-echo  $k$ -space data. In the case of gradient echoes,  $\rho_m$  is governed by

$$\rho_m = \left( \sum_i I_i \cdot e^{i2\pi f_i TE_m} \cdot e^{-R_{2,i}^* TE_m} \right) \cdot e^{i2\pi f_{B_0} TE_m}, \quad (2)$$

where the first term sums up signals from all chemical species (indexed by  $i$ ), characterized by their corresponding proton density ( $I_i$ ), resonance frequency ( $f_i$ ) and relaxation rate ( $R_{2,i}^*$ ). Here, the dependency on the spatial coordinates  $\vec{r}$  is suppressed for simplicity. In addition, the echo signal is modulated by the  $B_0$  field inhomogeneity.  $TE_m$  denotes the  $m$ th echo time.

This generalized multi-species signal can be simplified to only two compartments [10]–[12], i.e. water (W) and fat (F),

$$\rho_m = (W + F \cdot z_m) \cdot e^{-R_2^* TE_m} \cdot e^{i2\pi f_{B_0} TE_m}. \quad (3)$$

The chemical-shift phase modulation from fat is denoted as  $z_m$  with the 6-peak fat spectrum [11], while all fat peaks are assumed to have an equal  $R_2^*$  [35]. W and F are complex-valued, while  $R_2^*$  and  $f_{B_0}$  are constrained to be real.

Given the above MR signal models, the nonlinear forward model in multi-coil multi-echo acquisition can be written in the operator form

$$y_{j,m} = F_{j,m}(x) := P_m \mathcal{F} M S \mathcal{B}, \quad (4)$$

with  $x = (W, F, R_2^*, f_{B_0}, \dots, c_j, \dots)^T$ .  $F_{j,m}(x)$  denotes the forward operator.  $j$  is the the coil index ( $j \in [1, N_{\text{coil}}]$ ), and  $m$  the echo index ( $m \in [1, N_{\text{echo}}]$ ). The nonlinear operator ( $\mathcal{B}$ ) calculates echo images according to the parameter maps in  $x$  and the corresponding signal model as given in Equation (3). Every echo image is then point-wisely multiplied by every coil sensitivity map in  $x$ , as denoted by the operator  $S$ . Afterward, all multi-echo coil images are masked to be restricted to a given field of view (FOV) ( $M$ ), Fourier-transformed ( $\mathcal{F}$ ), and sampled ( $P$ ) at each echo. In addition, because radial sampling acquires  $k$ -space data within a circular region, the  $k$ -space filter [36] is applied to the sampling pattern to suppress potential checker-board artifacts.

### C. Model-based Nonlinear Inverse Reconstruction

The joint estimation of the unknown  $x$  is a nonlinear inverse problem,

$$\begin{aligned} & \text{minimize } \|y - F(x)\|_2^2 \\ & + \lambda_1 \|\mathcal{L}(E_1 x)\|_1 + \lambda_2 \|\text{TV}_t(E_2 x)\|_1 \\ & + \lambda_3 \|x\|_2^2 \end{aligned} \quad (5)$$

subject to  $R_2^* \geq 0$

The unknown  $x$  in this problem contains respiratory-motion-resolved model parameter maps (W, F,  $R_2^*$ , and  $f_{B_0}$ ) as well as coil sensitivity maps, and thus has the shape of  $[N, N, 4 + N_{\text{coil}}, N_{\text{bin}}]$ . Here,  $[N, N]$  corresponds to the image matrix size, 4 is the total number of model parameters, and  $N_{\text{bin}}$  is the number of respiratory bins.

R1.2

The locally low rank (LLR) regularization  $\mathcal{L}$  with the regularization strength  $\lambda_1$  was applied onto the parameters  $W$ ,  $F$  and  $R_2^*$ . These parameter maps were extracted from the complex  $x$  matrix using the operator  $E_1$ , which gets a sub-matrix from  $x$ . Note that regularization of echo images is not possible in model-based reconstruction, which formulates nonlinear inverse problems to directly estimate model parameter maps. The block size of the LLR constraint was  $16 \times 16$  with random shifts of the blocks among iterations.

**R1.2** For the reconstruction problems with a temporal dimension, the data consistency term in Equation (5) expands to include all temporal frames,  $\sum_t \sum_m \sum_j \|y_{j,m,t} - F_{j,m,t}(x)\|_2^2$ . Therefore, temporal TV regularization [38] with the regularization strength  $\lambda_2$  was applied onto all model parameter maps ( $W$ ,  $F$ ,  $R_2^*$ , and  $f_{B_0}$ ), which can be extracted via the operator  $E_2$ .

In addition,  $\ell^2$  regularization with the regularization strength  $\lambda_3$  was applied to all unknowns and a non-negativity constraint to the  $R_2^*$  map. To enforce spatial smoothness of the  $B_0$  and coil sensitivity maps, the Sobolev-norm weighting [28] was utilized to penalize high spatial frequencies,

$$T = \mathcal{F}^{-1} \left( 1 + w \cdot \|\vec{k}\| \right)^{-h} \quad (6)$$

$h$  is set as 16 for both maps, while  $w = 22$  and  $w = 220$  for the  $f_{B_0}$  and coil sensitivity maps, respectively.  $\vec{k}$  is a 2D Cartesian grid ranging from  $-0.5$  to  $0.5$  [30].

The objective functional in Equation (5) was solved by IRGNM with ADMM. For details about this algorithm please refer to Appendices I and II. Our implementation enables flexible selections of regularization terms.

We compared our proposed regularization strategy against only  $\ell^2$  regularization (i.e. removal of the  $\ell^1$  terms in Equation (5)) as well as the spatial TV regularization method (i.e. replacement of all regularization terms in Equation (5) by  $\lambda_4 \|\text{TV}_{\text{spatial}}(E_1 x)\|_1$ ) [16].

### III. METHODS

#### A. Phantom Experiments

A water/fat & iron phantom [39], [40] was constructed. Details of this phantom are provided in Fig. 2 and Table I. Due to steam coming from the water solution, which was heated at the hotplate at  $300^\circ\text{C}$  to create water and fat emulsion, the actual fat fraction was higher than prescribed in Table I. Therefore, the actual fat fraction values of every tube were validated using the standard Siemens MR spectroscopy (MRS) protocol.

**R2.2** MRI experiments were conducted with an 18-channel body matrix coil together with a spine coil on 3 T (Skyra, Siemens Healthineers, Erlangen, Germany). The proposed multi-echo radial sampling sequence was used with the following parameters: FOV 200 mm, base resolution 160, spatial resolution  $1.25 \text{ mm} \times 1.25 \text{ mm} \times 3.5 \text{ mm}$ , bandwidth 1040 Hz/pixel, flip angle  $4^\circ$ , asymmetric echo [41] of 30 %, TE 1.07, 2.35, 3.23, 4.51, 5.39, 6.67, 7.55 ms and TR 8.81 ms.

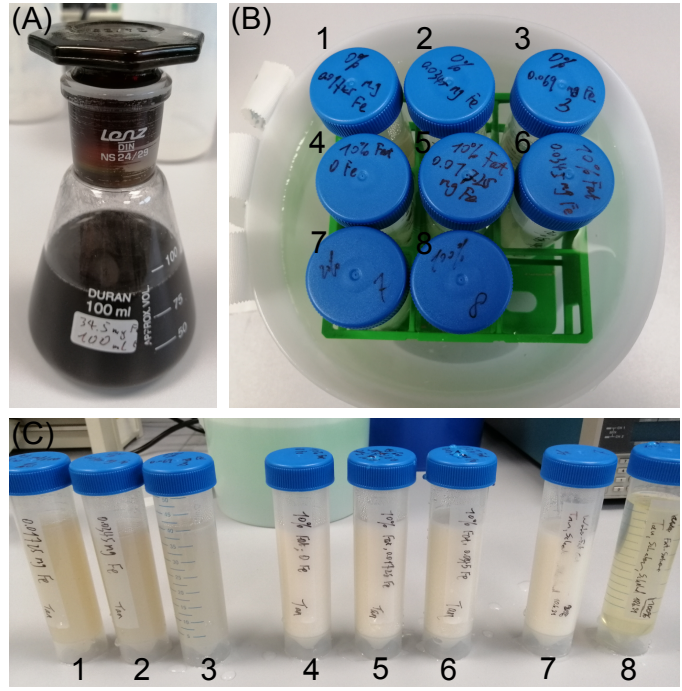


**Fig. 2.** Photos of the constructed water/fat & iron phantom. (A) 34.5 mg iron nano particle diluted in 100 mL distilled water. (B) Phantom layout with eight tubes as listed in (C).

#### B. In Vivo Experiments

For in vivo scans, the same coils and MRI system were used. Two radial protocols were implemented, one with a smaller field of view (FOV) 320 mm for subjects with relatively small body size (Volunteer #1), and another with a larger FOV 410 mm which fits well for obese patients (Patient #1 to #9). Breath-hold multi-echo Cartesian Dixon MRI was used as the reference. Detailed parameters are provided in Table II. Although the Cartesian scan requires one single breath hold and is fast, it captures only one motion state. In contrast, the proposed radial scan allows for free breathing, but requires longer scan time (2:47 min). Further, we investigated the effectiveness of the proposed motion-resolved model-based reconstruction on retrospectively undersampled radial data.

One volunteer and nine obesity/diabetes/NAFLD patients participated in our study. All subjects gave written informed consent before MRI in compliance with the regulations established by the local ethics committee. A summary of all subjects is given in Table III, including the age, gender, height, weight, and the body mass index (BMI).

#### C. Model-based Reconstruction

In the spirit of reproducible and open research, the proposed regularized model-based reconstruction is made publicly available in BART [42]. Scripts to produce the experiments are available at <https://github.com/mrirecon/multi-echo-liver> upon publication. A brief description of the reconstruction procedure is given here.

**Pre-Processing:** The acquired multi-coil multi-echo data was compressed to ten virtual coils via principal component

**TABLE I**  
MEASURED VOLUME OF IRON, WATER AND PEANUT OIL SOLUTIONS FOR THE EIGHT TUBES

Solution (mL)	Tube 1	Tube 2	Tube 3	Tube 4	Tube 5	Tube 6	Tube 7	Tube 8
Iron	0.5	1.0	2.0	0	0.5	1.0	0	0
Water	50	50	50	45	45	45	40	0
Fat	0	0	0	5	5	5	10	50

**TABLE II**

IMAGING PARAMETERS FOR (LEFT) THE BREATH-HOLD CARTESIAN REFERENCE AND (RIGHT) THE PROPOSED FREE-BREATHING MULTI-ECHO RADIAL ACQUISITION WITH TWO DIFFERENT FOV

	Cartesian	Radial	Radial
Flip angle ( $^{\circ}$ )	4	4	4
Bandwidth (Hz/pixel)	1080	1090	1090
Asymmetric echo	None	30 %	30 %
Number of echoes	6 <sup>a</sup>	7 <sup>b</sup>	7 <sup>c</sup>
Repetition Time (ms)	9	8.35	8.39
FOV (mm $\times$ mm)	410 $\times$ 348	320 $\times$ 320	410 $\times$ 410
Pixel size (mm $\times$ mm)	2.56 $\times$ 2.56	1.6 $\times$ 1.6	1.6 $\times$ 1.6
Base resolution	160	200	256
Slice thickness (mm)	3.5	3.5	3.5
Slice resolution (%)	50	100	100
Slice oversampling (%)	25	25	25
Number of slices	64	48	48
Scan time (min:sec)	0:20	2:45	2:47

<sup>a</sup> Echo times are 1.06, 2.46, 3.69, 4.92, 6.15, 7.38 ms;

<sup>b</sup> Echo times are 0.98, 2.20, 3.04, 4.26, 5.10, 6.32, 7.16 ms;

<sup>c</sup> Echo times are 0.98, 2.21, 3.05, 4.28, 5.12, 6.35, 7.19 ms.

**TABLE III**  
SUMMARY OF SUBJECTS PARTICIPATED IN THE STUDY

	Age	Gender	Height (cm)	Weight (kg)	BMI (kg/m <sup>2</sup> )
Volunteer #1	27	F	155	60	25.0
Patient #1	55	M	184	105	31.0
Patient #2	60	F	172	105	35.5
Patient #3	64	F	164	80	29.7
Patient #4	60	F	153	112	47.8
Patient #5	44	F	165	94	34.5
Patient #6	43	F	165	165	60.6
Patient #7	65	M	176	98	31.6
Patient #8	55	F	156	88	36.2
Patient #9	54	F	160	68	26.6

analysis [43]. The multi-echo sampling trajectory was corrected for gradient delays using the radial spoke intersections for gradient delay estimation (RING) method [44]. RING determines the intersection points of different radial spokes. Afterward, RING estimates the gradient delay coefficients given the position of the intersection points. RING was applied to every echo to estimate its corresponding gradient delay coefficients, which were then used to correct for trajectories.

**Binning:** In this work, the singular spectrum analysis (SSA-FARY) technique [45] was adapted for self-gating of respiratory motions. SSA-FARY combines the ideas of time-delayed embedding and principle component analysis, and allows for robust extraction of oscillatory motion signals such as respiration from an auto-calibration (AC) region. In particular, for a periodic signal contained in the AC region, SSA-FARY yields a quadrature pair, which can be used for self-gating. Such a quadrature pair can be thought of as a generalized sine-cosine-pair describing the respective periodic

motion and can be represented by a phase-portrait, where an angle of  $0^{\circ}$  states the beginning and  $360^{\circ}$  states the end of a motion cycle.

In this work, we chose to split the respiratory motion into four bins, hence, each bin represents a circular sector with a central angle of  $360^{\circ}/N$ . Then, the respiratory motion state at a given time is determined by the respective angle defined by the quadrature pair. As one echo train was relatively short, only the first echo was extracted for SSA-FARY.

Note that although more respiratory bins can improve the temporal resolution, it leads to fewer radial spokes per bin. Such a trade-off can be alleviated via the temporal TV regularization. However, we observed that increasing bins did not significantly affect the reconstructed image quality (results not shown). Therefore, we chose four respiratory bins in this study. Since the reference Cartesian scan was performed during end expiration, we used the end-expiration bin of the radial scan for comparison.

**Initialization:** Off-resonance phase modulation causes phase wrapping along the echoes, especially in the case of large  $B_0$  field inhomogeneity. Consequently, multiple local minima could occur for the field map  $f_{B_0}$ . To prevent this, the  $f_{B_0}$  map was initialized from a model-based three-point water/fat separation [30]. W and F were initialized as 0.1.  $R_2^*$  and coil sensitivity maps were initialized as 0.

**Iterative Reconstruction:** For the model-based reconstruction, the regularization strength in Equation (5) (e.g.  $\lambda_1$ ,  $\lambda_2$ , and  $\lambda_3$ ) is reduced along Newton steps, e.g.  $\lambda_1^{(n)} = 1/D^{n-1}$  for  $\lambda_1$ , with  $n$  being the  $n$ th Newton iteration and the reduction factor  $D > 1$ .  $D = 3$  was used in this work. For ADMM, the maximum number of iterations in each Newton iteration were given as:  $n_{\text{maxiter}} = \min(M, 10 \times 2^{-\ln \lambda^{(n)}})$ , where  $M$  can be specified by the user (200 as default). Consequently, the maximal iterations gradually increase along the Newton steps.

In this work, eight Newton steps were employed, and the ADMM penalty parameter  $\rho$  was set as 0.001. For the regularization terms in Equation (5), we set  $\lambda_1 = 0.0003$ ,  $\lambda_2 = 0.1$ , and  $\lambda_3 = 1$ . The scaling of the F,  $R_2^*$ , and  $B_0$  maps was set as 1.6, 0.001, and 1, respectively. All reconstructions were performed on a Tesla V100-SXM2 32 GB GPU (NVIDIA, Santa Clara, CA, USA).

**Post-Processing:** With the reconstructed water and fat images, fat fraction (FF) maps can be computed taking into account the magnitude discrimination [46], i.e.  $FF = 1 - |W|/(|W| + |F|)$  for pixels in which water dominates.

#### IV. RESULTS

With the proposed multi-echo radial FLASH acquisition and model-based reconstruction, Fig. 3 shows the results of the in-house built water/fat & iron phantom. The FF values of every

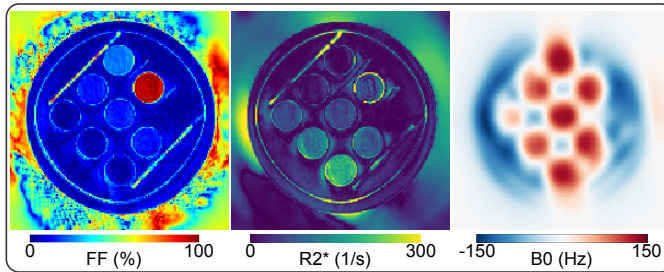


**Fig. 3.** Multi-echo radial FLASH acquisition and model-based reconstruction results of the water/fat & iron phantom built in-house. Displayed images are FF,  $R_2^*$ , and  $B_0$  maps, respectively.

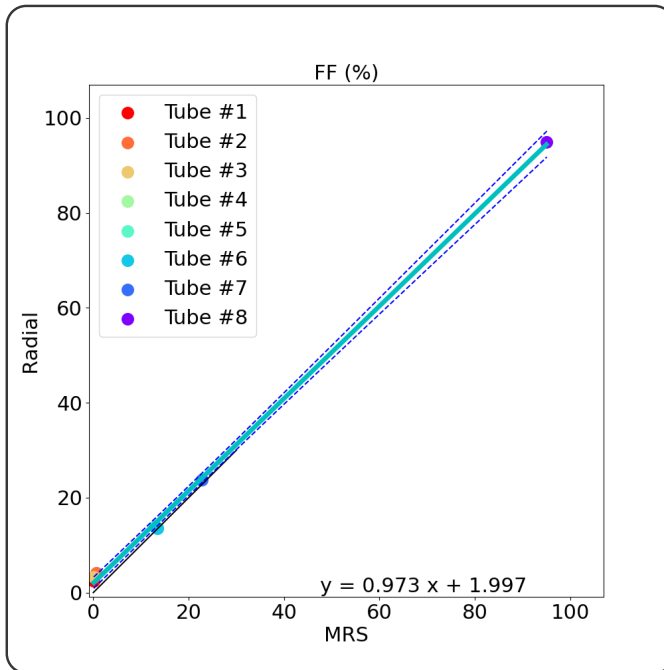


**Fig. 4.** Quantitative analysis of FF values for the eight tubes via linear regression between the standard MR Spectroscopy (MRS) and the proposed multi-echo radial acquisition with model-based reconstruction. Tube 8 (filled with peanut oil) is excluded for the analysis due to the lack of its MRS measurement.

tube are validated against the MRS measurements. The FF values of all tubes match well between the two measurements, as shown in Fig. 4.

Fig. 5 shows the reconstructed FF and  $R_2^*$  maps of Patients #1 and #2 from the reference breath-hold Cartesian and the proposed free-breathing radial scan, respectively. The  $R_2^*$  maps from Cartesian scans suffer from noise in the middle region (likely due to undersampling in the phase-encoding direction). Moreover, as pointed out by the yellow arrows, incomplete breath hold results in artifacts in the  $R_2^*$  maps. For model-based reconstructions of the radial scan, three regularizations of the parameter maps (W, F and  $R_2^*$ ) were compared:  $\ell^2$ , spatial TV (as employed by Schneider et al. [16]), and LLR plus temporal TV proposed in this work. The application of LLR plus temporal TV regularization outperforms both the  $\ell^2$  and the spatial TV regularizations, as evident by the reduced streaking artifacts and better delineation of the liver. All subsequent figures use the same color maps for FF and

$R_2^*$  as in Fig. 5.

Further, to demonstrate the effectiveness of using SSA-FARY for the motion resolved free-breathing radial scan, Fig. 6 compares the reference breath-hold Cartesian scan and the proposed free-breathing radial scan for Patient #1 in the reformatted coronal view. While the liver dome region shows hyper  $R_2^*$  intensity from the Cartesian scan, consistent  $R_2^*$  values are visible from the proposed radial scan and model-based reconstruction. Such hyper intensity may be caused by the fast  $B_0$  field change in the liver dome region, which is close to the lung with much lower MR signal. On the other hand, respiratory motion is well separated across the four frames. As shown in the self-gating AC signal plot in Fig. 6 (B), A total of 330 radial spokes were acquired during the free-breathing scan. When plotted into the phase portrait, the pair of empirical orthogonal functions (EOF) can be equally divided into four angular blocks, representing four distinct respiratory motion states.

**TABLE IV**  
SUMMARY OF FF VALUES FOR ALL PATIENTS FROM THE REFERENCE CARTESIAN AND THE PROPOSED RADIAL ACQUISITION.

	Cartesian	Radial (2:47)	Radial (1:24)
Patient #1	25.07 ± 2.55	26.81 ± 3.62	25.83 ± 4.28
	19.66 ± 1.92	19.62 ± 3.73	20.47 ± 3.67
	21.28 ± 1.79	23.50 ± 2.32	24.54 ± 2.39
Patient #2	21.52 ± 2.17	21.53 ± 2.34	18.56 ± 4.02
	20.79 ± 1.81	20.56 ± 3.08	18.43 ± 4.05
	20.56 ± 1.24	23.58 ± 1.33	22.98 ± 1.69
Patient #3	13.66 ± 2.31	12.85 ± 2.79	15.36 ± 3.88
	13.64 ± 3.15	14.61 ± 3.42	16.44 ± 3.65
	14.95 ± 1.76	18.74 ± 3.52	19.89 ± 4.04
Patient #4	13.18 ± 3.55	13.12 ± 5.28	13.64 ± 5.97
	13.41 ± 3.11	13.34 ± 2.91	13.92 ± 3.52
	14.37 ± 3.04	15.17 ± 1.99	15.45 ± 2.27
Patient #5	16.77 ± 1.35	17.51 ± 0.99	13.31 ± 1.66
	19.33 ± 1.22	18.74 ± 1.29	16.86 ± 1.69
	17.34 ± 2.05	17.89 ± 1.79	17.04 ± 1.87
Patient #6	7.82 ± 2.90	5.47 ± 2.54	7.98 ± 3.73
	4.82 ± 2.03	4.87 ± 2.12	6.87 ± 2.58
	7.39 ± 1.23	6.70 ± 1.50	8.52 ± 2.45
Patient #7	9.44 ± 1.28	11.83 ± 1.85	9.34 ± 3.12
	11.24 ± 1.27	13.63 ± 1.70	13.62 ± 2.90
	12.18 ± 1.59	13.96 ± 2.26	13.36 ± 3.22
Patient #8	17.87 ± 3.10	16.71 ± 2.02	16.45 ± 3.71
	14.16 ± 1.35	14.94 ± 3.71	14.76 ± 4.01
	14.80 ± 1.40	16.42 ± 1.63	16.79 ± 2.89
Patient #9	26.60 ± 0.76	29.02 ± 1.66	28.71 ± 2.19
	26.85 ± 0.98	29.24 ± 2.21	28.95 ± 2.85
	27.45 ± 1.05	30.31 ± 1.53	30.08 ± 2.34

Fig. 7 depicts the Bland-Altman as well as scatter plots comparing the reference breath-hold Cartesian scan and the proposed free-breathing radial scan. For this quantitative analysis, three regions of interest (ROI) were selected for every subject and the mean value of every ROI was used for plotting. In the Bland-Altman plots, the x and y axis represents the mean and difference values between these two scans, respectively. The central dotted line along the x-axis shows the mean bias between these two scans and is computed by averaging the difference values. The upper and lower dotted lines show the limits of agreement (mean bias ± 1.96 × standard deviation of difference). In the scatter plots, the x and y axis represents the mean values of the Cartesian and the radial scan, respectively.

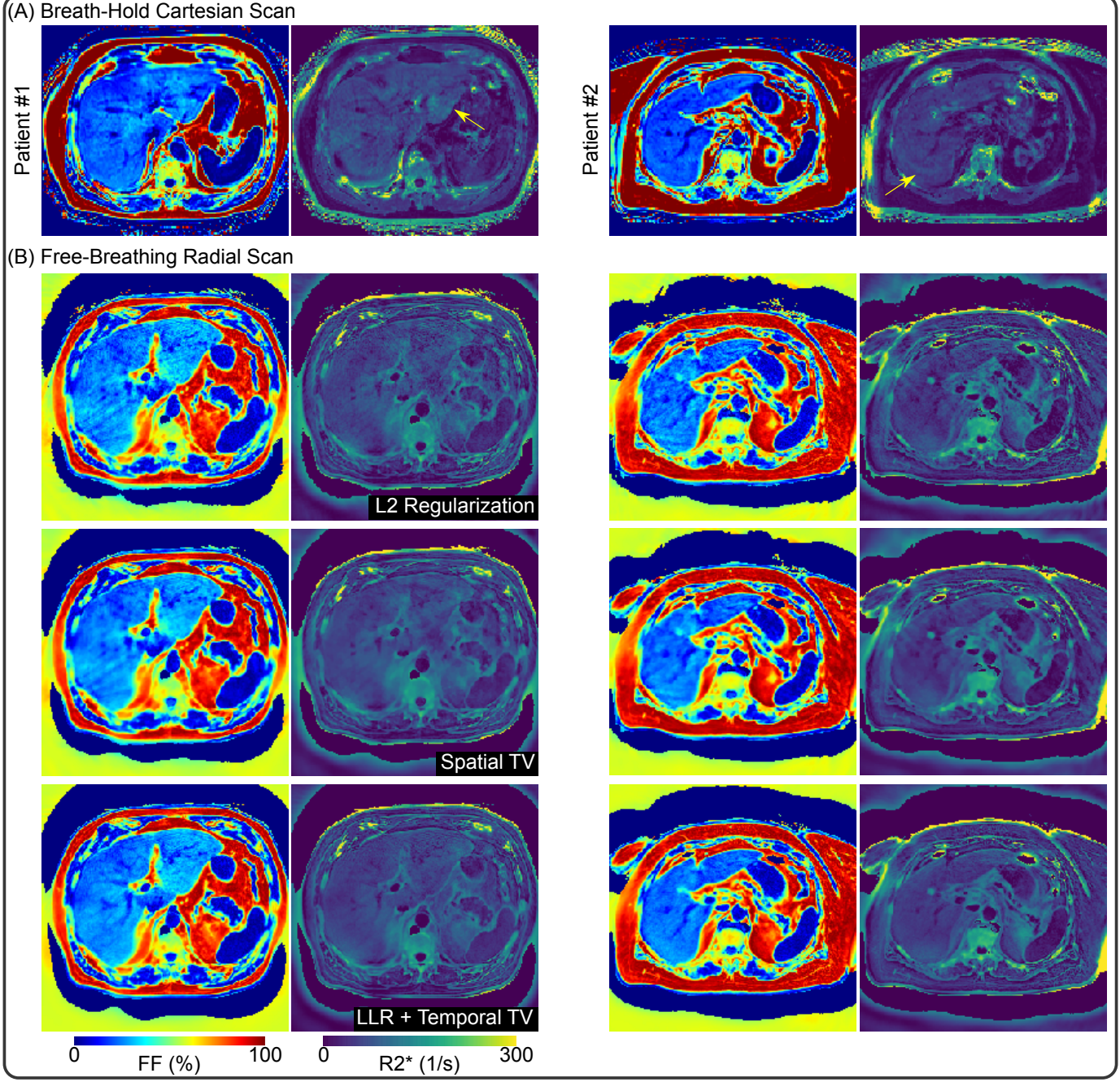


**Fig. 5.** Comparison of (A) the reference breath-hold Cartesian scan and (B) the proposed free-breathing radial scan on Patients #1 and #2. Furthermore, for the radial data in (B), we compared three different regularizations: L2 regularization, spatial TV regularization as used by Schneider et al. [16], and the proposed LLR and temporal TV regularization.

In addition, linear regression was performed. The slope of the fitted curve for both FF and  $R_2^*$  values is close to 1, indicating a good match between the Cartesian and the radial measurements.

Tables IV and V further summarize both the mean and the standard deviation values of every ROI and every patient. Overall, the patients in this work cover wide ranges of FF and  $R_2^*$  values, and hence are representative for the validation of the proposed method. Moreover, the quantitative analysis results reveal two important clinical indications.

First, obese patients may not necessarily have fatty liver

disease. Patient #6 is diagnosed with obesity, and shows the highest BMI in Table III. For this patient, however, ultrasound is not able to penetrate through the thick subcutaneous fat layer to assess the liver fat content. As shown in Fig. 8, both breath-hold Cartesian and free-breathing radial scans are able to provide quantitative FF and  $R_2^*$  maps. The liver regions exhibit relatively low FF values. This patient shows the lowest FF and  $R_2^*$  values among all subjects in this study (see Fig. 7). On the other hand, the  $R_2^*$  maps in both the transversal and sagittal views again suffer from hyper intensities in the Cartesian scan (as pointed by yellow arrows), while our proposed radial scan

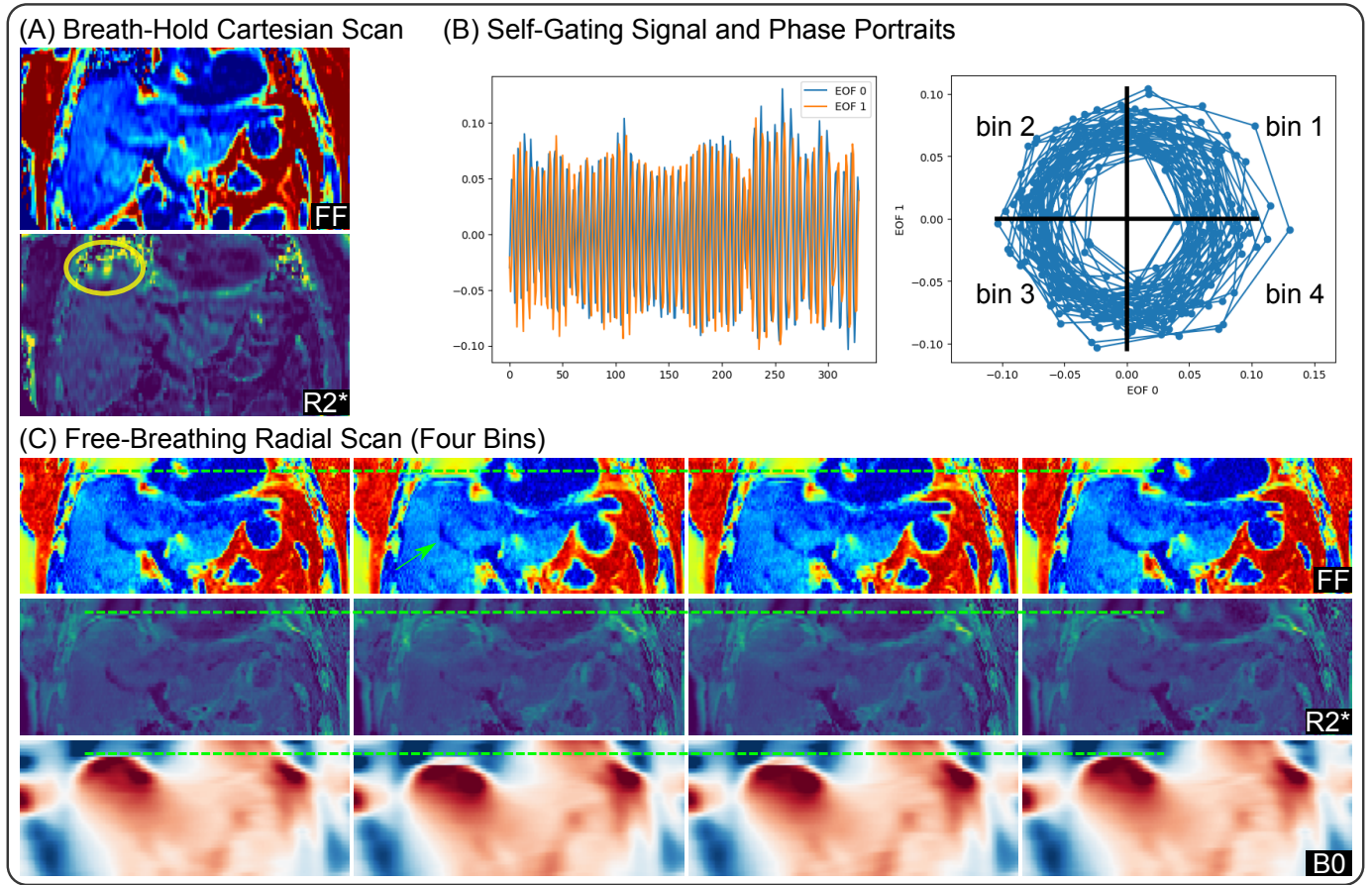


**Fig. 6.** (A) One coronal-view FF and  $R_2^*$  map from breath-hold Cartesian scan of Patient #1. (B) Plots of self-gating signal and phase portraits. (C) Four coronal-view FF and  $R_2^*$  maps from free-breathing radial scan with self-gated motion-resolved model-based reconstruction. The  $R_2^*$  map in (A) suffers from hyper intensities in the liver dome region (yellow ellipse), whereas the proposed radial scan shows consistent  $R_2^*$  values.

shows more homogeneous  $R_2^*$  maps.

Second, in our study, patients with hepatic steatosis may not necessarily be obese. Fig. 9 displays one volunteer and one patient with elevated FF values from both the reference breath-hold Cartesian and the free-breathing radial scans. Patient #9 was even confirmed about hepatic steatosis via the standard liver biopsy and ultrasound diagnosis. However, neither of them shows the problem of obesity (see Table III). Through Fig. 7 and Fig. 9, we also observe that hepatic steatosis is more likely to occur in elderly patients. Although fatty liver is also captured in the scan of Volunteer #1, this is rather a rare case among all young volunteers (results now shown here). On the other hand, in the left corner of the liver in Patient #9 (see the green arrows),  $R_2^*$  values from the Cartesian scan again are higher, possibly due to the fast  $B_0$  change in this air-tissue interface, created by the empty region within the stomach.

Noteworthy, the reference Cartesian scan requires subjects to hold their breath. When subjects fail to perform breath holding, it may lead to image artifacts in the reconstruction. Figs. 9 and 10 (see yellow arrows) are such examples. Residual respiratory motion during the scan causes fast  $B_0$  field drift [30] as well as signal variation. This situation makes the fitting of  $B_0$  and  $R_2^*$  difficult. In this example, it results in the blurring artifact for Patient #3 and ripple-like artifact for Patient #8 (see yellow arrows) and unreliable  $R_2^*$  values. However, the

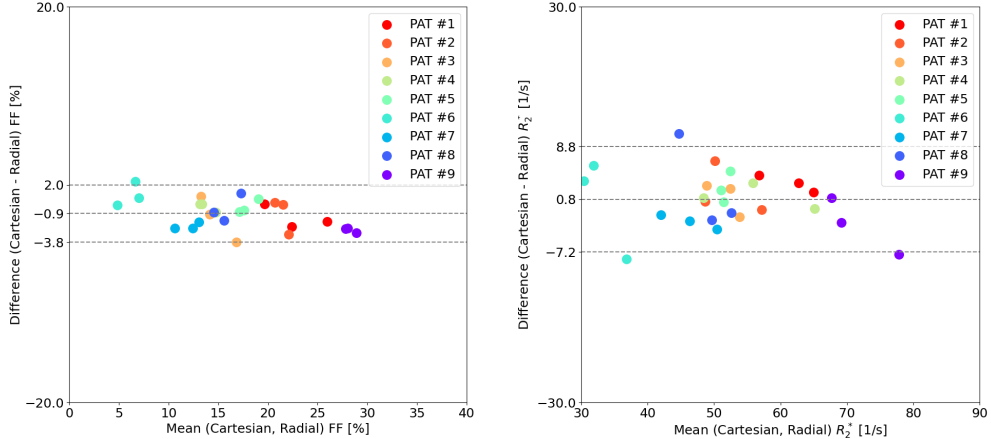
proposed free-breathing radial scan is free of such artifacts.

Furthermore, we investigated reducing the acquired radial data by one-half, to explore the feasibility of the proposed motion-resolved model-based reconstruction on retrospectively undersampled data. As shown in Figs. 10 and 11 as well as in the right column of Tables IV and V, retrospective undersampling increases standard deviation in the reconstructed FF and  $R_2^*$  maps, but the mean values agree well with the reconstruction on the 2:47 min scan (the center column).

## V. DISCUSSION

This work introduced a stack-of-radial multi-echo radial FLASH sequence with partial Fourier readouts (i.e. asymmetric echo) for volumetric free-breathing liver acquisition. Moreover, this work introduced a regularized model-based reconstruction in BART to jointly estimate liver water, fat,  $R_2^*$ ,  $B_0$  field inhomogeneity maps, and coil sensitivity maps directly from acquired  $k$ -space data. This nonlinear inverse problem was solved by IRGNM with ADMM, allowing for generalized regularization terms in nonlinear reconstruction. To validate the proposed MRI sequence and reconstruction, a pilot study was conducted comprising young volunteers and patients diagnosed with obesity, diabetes, or hepatic steatosis. The reconstructed FF and  $R_2^*$  maps were further compared with the reference breath-hold Cartesian scan. We found good

(A) Bland-Altman plots comparing breath-hold Cartesian and free-breathing radial scans



(B) Linear regression between breath-hold Cartesian and free-breathing radial scans

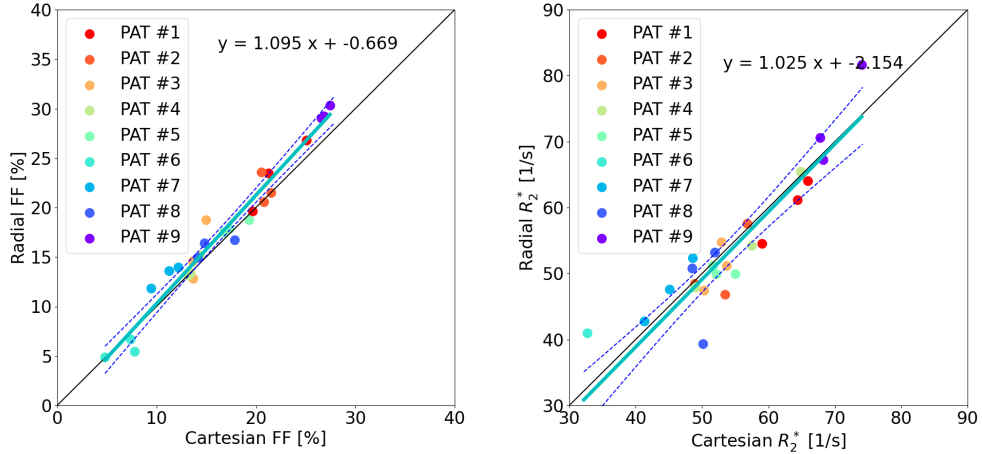


**Fig. 7.** Quantitative analysis of reconstructed FF and  $R_2^*$  maps for all subjects comparing the reference breath-hold Cartesian scan and the proposed free-breathing radial scan, respectively.

agreement between the proposed free-breathing radial scan and the breath-hold Cartesian scan.

#### R2.3

The  $R_2^*$  maps of Patient #1 from the proposed method are visually more blurred compared to the reference Cartesian scan, while the volunteer  $R_2^*$  map shows a sharp delineation of the liver and vessel borders. This may be due to the use of a larger FOV in the acquisition protocol for patients, which corresponds to higher undersampling. On the other hand, the larger body size of this patient may result in poorer receiver signals in the middle.

#### R2.7

In model-based reconstructions, parameter maps are directly reconstructed from acquired  $k$ -space data. Therefore, regularizations can be directly imposed on parameter maps. An alternative approach is to reconstruct all echo images and then perform image-space parameter fitting [6]–[8], [20], [22]. In this case, advanced regularizations (e.g.  $\ell^1$ -Wavelet and low rankness) can be employed along the echo dimension. However, this study mainly focused on the comparison with the reference breath-hold Cartesian scan. In addition, this study also compared against another model-based reconstruction approach using spatial total variation regularization on parameter

maps [16]. It is evident in Fig. 5 that spatial TV regularization on the parameter maps can result in the ink-type artifact, whereas temporal TV regularization is beneficial to remove streaking artifacts.

This work initialized the  $B_0$  field inhomogeneity map for every respiratory bin by the  $B_0$  estimate from a 3-echo model-based reconstruction. As only three echoes were used for the reconstruction, this initialization procedure is relatively fast. Such  $B_0$  initialization assures the convergence of large-scale model-based reconstructions on seven echoes and four respiratory bins. Recently, Zhang et al. proposed the solution interval method for nonlinear inverse problems [47]. However, abundant computation power is required to run the nonlinear least square fitting multiple times for the construction of solution intervals for every unknown.

There are several aspects of this study that can be further improved. No patient participated in this study showed symptoms of iron overload (i.e. elevated  $R_2^*$  values). To the best of our knowledge, iron overload is more likely to be seen in patients who require regular blood transfusions. These patients, however, are rather rare in obesity/diabetes clinics.

#### R3.3

TABLE V

SUMMARY OF  $R_2^*$  VALUES FOR ALL PATIENTS FROM THE REFERENCE CARTESIAN AND THE PROPOSED RADIAL ACQUISITION.

	Cartesian	Radial (2:47)	Radial (1:24)
Patient #1	65.93 ± 9.69	64.08 ± 11.38	56.72 ± 14.78
	59.00 ± 7.67	54.56 ± 9.76	54.21 ± 13.88
	64.37 ± 8.05	61.13 ± 7.22	70.36 ± 8.63
Patient #2	56.76 ± 4.63	57.58 ± 13.52	44.44 ± 22.44
	53.43 ± 6.51	46.80 ± 4.88	48.66 ± 5.86
	48.90 ± 6.77	48.46 ± 4.23	62.61 ± 5.87
Patient #3	50.30 ± 9.98	47.42 ± 9.91	43.57 ± 14.45
	53.66 ± 11.92	51.20 ± 8.97	52.30 ± 11.97
	52.94 ± 9.15	54.81 ± 10.26	60.57 ± 11.76
Patient #4	57.52 ± 13.85	54.21 ± 13.28	59.46 ± 14.17
	48.93 ± 17.38	47.89 ± 6.67	47.05 ± 7.71
	64.83 ± 8.66	65.47 ± 5.54	60.13 ± 6.56
Patient #5	52.17 ± 6.65	49.96 ± 4.98	48.01 ± 4.81
	51.61 ± 6.70	51.22 ± 2.96	52.09 ± 3.83
	55.00 ± 6.23	49.92 ± 3.57	52.25 ± 5.25
Patient #6	32.71 ± 8.34	40.98 ± 8.37	39.14 ± 11.56
	32.20 ± 5.82	28.62 ± 3.38	27.12 ± 6.21
	34.83 ± 5.85	28.93 ± 2.94	25.97 ± 3.92
Patient #7	41.27 ± 6.39	42.79 ± 5.27	42.40 ± 10.18
	48.56 ± 4.66	52.34 ± 3.92	46.31 ± 7.66
	45.07 ± 4.13	47.59 ± 6.75	50.20 ± 7.36
Patient #8	48.50 ± 10.91	50.84 ± 6.26	51.40 ± 8.10
	50.11 ± 6.90	39.33 ± 13.85	43.56 ± 15.84
	51.94 ± 4.19	53.21 ± 5.36	50.50 ± 7.45
Patient #9	68.23 ± 3.42	67.24 ± 10.13	72.99 ± 14.40
	67.82 ± 4.67	70.57 ± 8.16	74.60 ± 10.89
	74.05 ± 4.03	81.62 ± 6.64	77.14 ± 11.25

Although lacking real patients, we showed the capability of our technique in quantifying iron overload in the phantom, as seen in Fig. 3, where Tube 3 results in the highest  $R_2^*$  value due to iron.

Joint estimation of all physical parameter maps and coil sensitivity maps is a nonlinear nonconvex inverse problem. Especially when including the  $B_0$  field inhomogeneity map as one unknown, the reconstruction is sensitive to the initial guess and scaling of unknowns. Our implementation initialized the  $B_0$  map with the previously proposed three-echo reconstruction [30], which indeed fostered convergence. Second, scaling of the fat,  $R_2^*$ , and  $B_0$  maps was empirically determined. Therefore, more intelligent  $B_0$  estimation and automatic scaling of unknowns [48] would be logical directions.

Compared with the reference breath-hold Cartesian scan, our proposed radial sampling did not explore  $k_z$  unaligned undersampling strategies [49], which can further accelerate data acquisition.

While this work focused on liver fat and  $R_2^*$  mapping, the presented multi-echo radial sequence in principle is also applicable to brain imaging, which, would become rather interesting in combination with the above-mentioned  $k_z$  undersampling. Alternatively, one can also explore the possibility of multiple parametric mapping via extending the basic multi-echo radial acquisition to variable flip angles or magnetization preparation.

This work employed the recently proposed SSA-FARY technique for self-gating, where the determination of spokes as respiratory bins was based on polar angles in the phase portrait plot. This procedure did not take into account the radius of every spoke in phase portrait, which might cause problems in the case of irregular breathing. Therefore, it might make

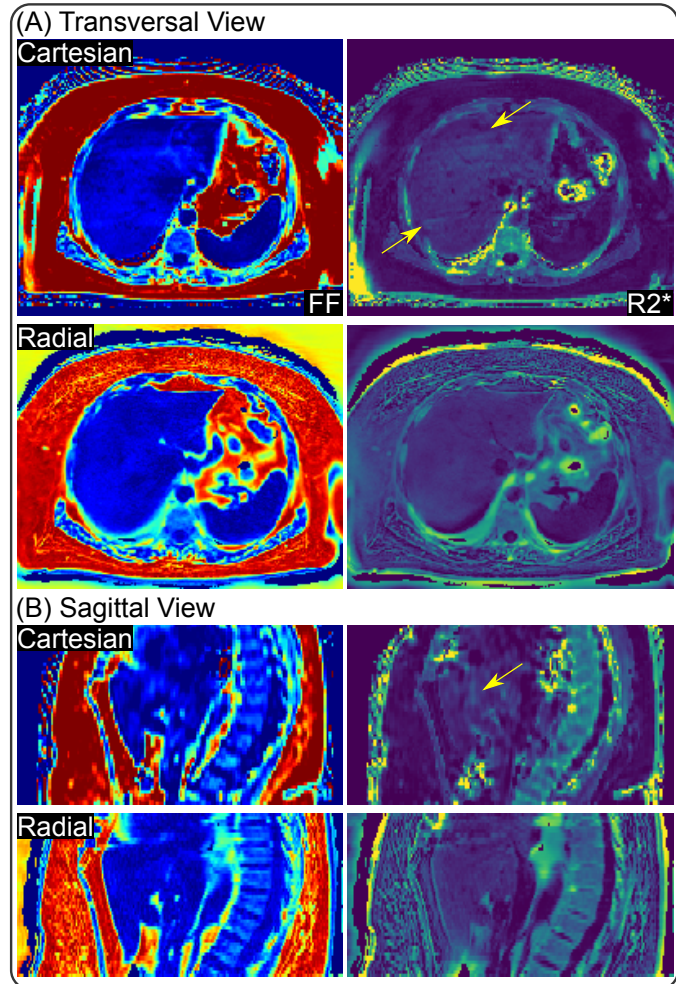


Fig. 8. (A) Transversal view and (B) sagittal view of reconstructed FF and  $R_2^*$  maps in Patient #6 comparing the reference breath-hold Cartesian scan and the proposed radial scan, respectively. This patient shows definite obesity symptom (see Table III), but has no fatty liver. In fact, the FF values of this patient is the lowest among all subjects (see also Fig. 7). Similar to the results of Patient #1 in Fig. 5, the Cartesian scan suffers from fold-in artifacts in the  $R_2^*$  maps (yellow arrows), while the proposed radial scan shows consistent  $R_2^*$  values.

the self-gating technique more general considering the radius. Alternatively, it would be interesting to use pilot tone [50] for prospective respiratory binning during data acquisition.

The total reconstruction time for the whole liver took about 4 h on the Tesla V100 GPU. For clinical translation, further acceleration could be achieved via for example  $k_z$  undersampling, multiple GPU parallelization, and pre-calibrated coil sensitivity maps. These aspects, however, are outside the scope of this work, which mainly focused on the technical development of the free-breathing model-based reconstruction method.

## VI. CONCLUSION

This work introduced a free-breathing liver fat and  $R_2^*$  quantification technique, comprising stack-of-radial multi-echo asymmetric-echo acquisition and regularized model-based reconstruction. The generic model-based reconstruction framework in BART allows for generalized regularization

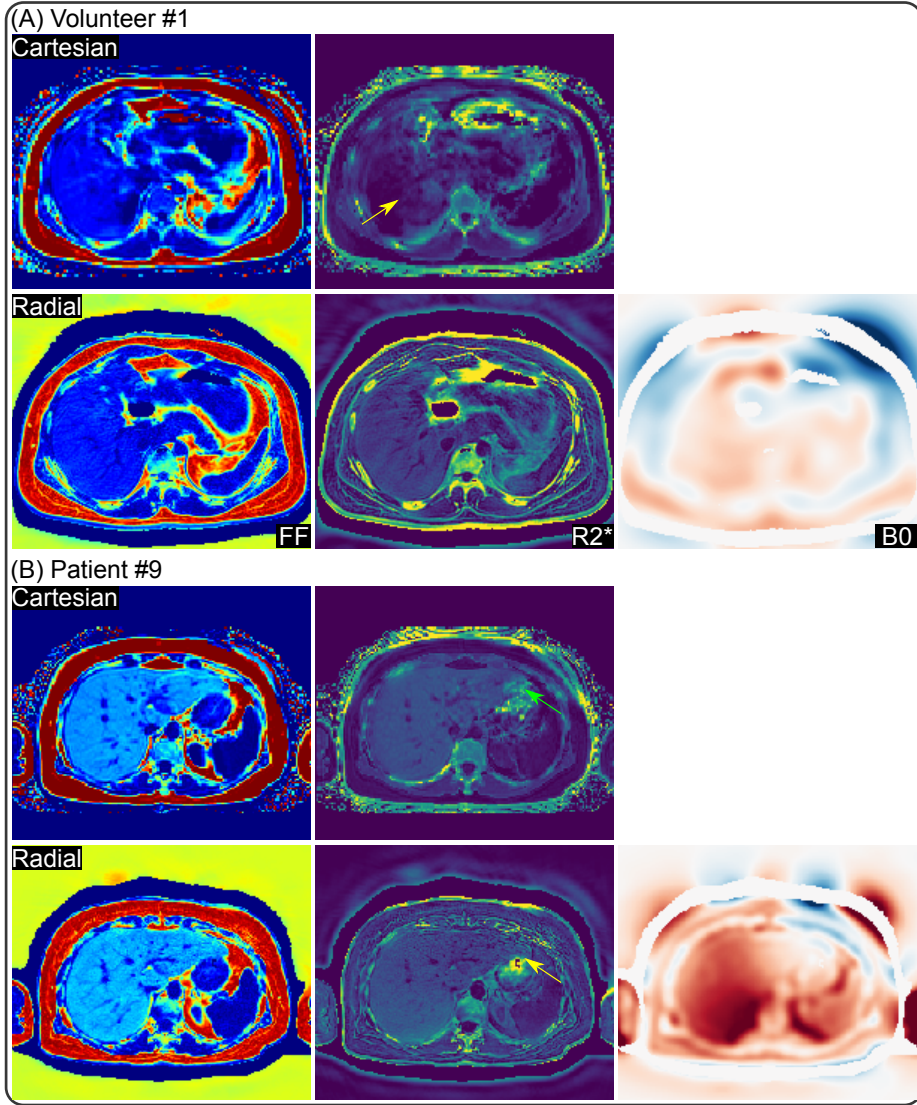


**Fig. 9.** (A) Volunteer #1 and (B) Patient #9 with elevated FF values, but no clear symptom of obesity. In particular, Patient #9 was diagnosed with hepatic steatosis by the standard liver biopsy and ultrasound.

terms and is integrable with different physical models. This work demonstrated the computational power of the proposed nonlinear inverse reconstruction framework, in which multiple temporal frames of the physical parameter maps (water, fat,  $R_2^*$ , and  $B_0$ ) and coil sensitivity maps are jointly estimated. This technique offers a non-invasive and non-physiological-gated tool for liver assessment.

#### APPENDIX I

To minimize the cost function in Equation (5), IRGNM linearizes the nonlinear forward model via Taylor expansion in each Newton step, thus the data-consistency term in Equation (5) becomes

$$\|DF(x_n)dx - [y - F(x_n)]\|_2^2 \quad (\text{A.1})$$

where the Jacobian  $DF(x_n)$  denotes the derivative of the forward operator concerning the  $n$ th-step estimate. Given the initial guess as  $x_0$  [28], one can denote  $x = x_{n+1} - x_0 =$

$x_n + dx - x_0$ . As a result, Equation (A.1) becomes

$$\begin{aligned} & \|DF(x_n)(x + x_0 - x_n) - [y - F(x_n)]\|_2^2 \\ & \Rightarrow \|DF(x_n)x - [DF(x_n)(x_n - x_0) + y - F(x_n)]\|_2^2 \end{aligned} \quad (\text{A.2})$$

whose minimum occurs when its derivative is set to 0, and we obtain such a linear system equation,

$$Ax = b \quad (\text{A.3})$$

for which we denote  $A := DF^H(x_n)DF(x_n)$  and  $b := DF^H(x_n)\{DF(x_n)(x_n - x_0) + y - F(x_n)\}$ .

With generalized  $\ell_1$  regularization, Equation (A.3) can be written in the ADMM form,

$$\begin{aligned} & \text{minimize } \|Ax - b\|_2^2 + \alpha \|z\|_1 \\ & \text{subject to } Tx - z = 0 \end{aligned} \quad (\text{A.4})$$

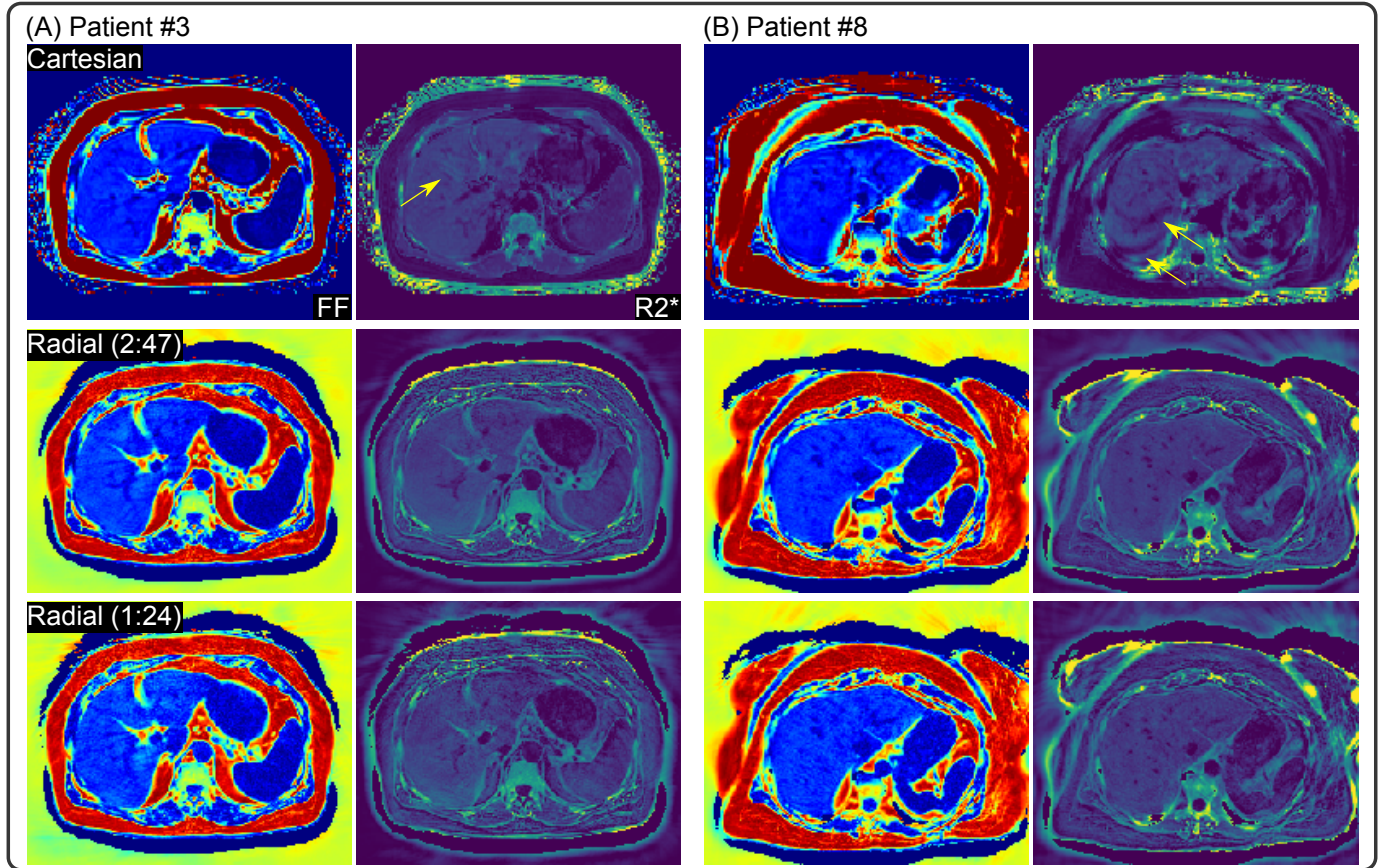


**Fig. 10.** Comparison of FF and  $R_2^*$  maps for Patients (A) #3 and (B) #8 among the reference Cartesian scan, the free-breathing radial 2:47 min scan, and the free-breathing radial scan with retrospective two-fold undersampling. Note the ripple-like artifact in the  $R_2^*$  map from the Cartesian scans due to incomplete breath hold (yellow arrows in the 1st row).

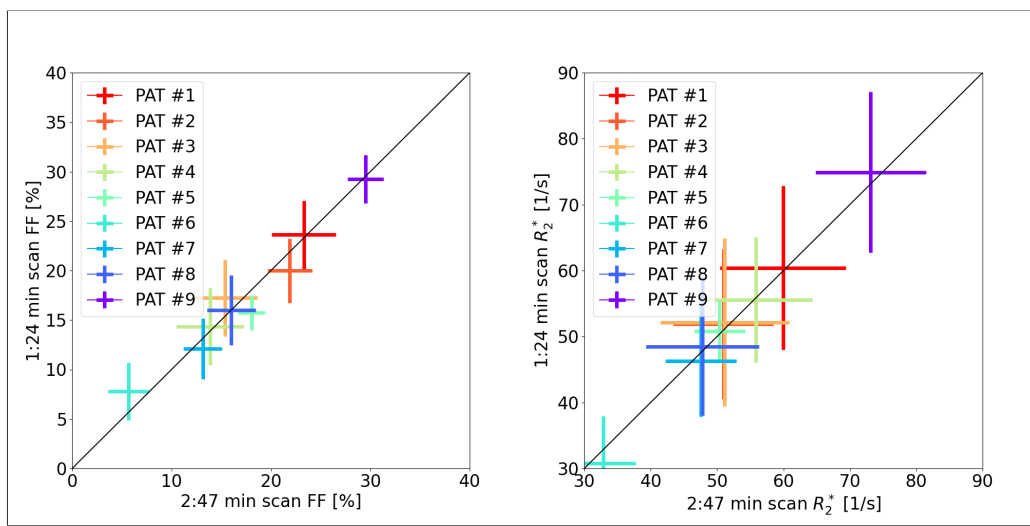


**Fig. 11.** Quantitative analysis of the reconstructed FF and  $R_2^*$  maps from radial scans: actual acquisition (2:47 min) and retrospectively undersampled acquisition (1:24 min), respectively.

The updates can be derived,

$$\begin{cases} x^{(k+1)} := (A^H A + \rho T^H T / 2)[A^H b + \rho T^H(z^{(k)} - \mu^{(k)}) / 2] \\ z^{(k+1)} := \mathcal{T}_{\alpha/\rho}(T x^{(k+1)} + \mu^{(k)}) \\ u^{(k+1)} := u^{(k)} + T x^{(k+1)} - z^{(k+1)} \end{cases} \quad (\text{A.5})$$

The  $x$  update is solved by the conjugate gradient method, and the  $z$  update is computed via soft thresholding ( $\mathcal{T}_{\alpha/\rho}$ ), where  $\alpha$  is passed from IRGNM and iteratively reduced along Newton steps,  $\alpha = 1/D^{n-1}$  with  $D > 1$  and  $n$  the  $n$ th Newton iteration.  $\rho$  is known as the penalty parameter in ADMM.

## APPENDIX II

The iterative solution to Equation (A.3) requires the computation of the Jacobian  $DF(x)$  and its corresponding adjoint  $DF^H(x)$  operator, with the forward operator  $F(x)$  denoted in Equation (4). Note that the forward operator can be split into two nonlinear operators: the parallel imaging operator ( $P\mathcal{FMS}$ ) and multi-echo signal model operator ( $\mathcal{B}$ ). Since the first one has already been implemented in BART for parallel imaging as nonlinear inversion (NLINV) [28], only the second operator is required to be implemented. Afterward, the two nonlinear operators can be chained together. Therefore, only the operator  $\mathcal{B}$  is explained in detail here.

As denoted in Equation (3), the nonlinear operator  $\mathcal{B}$  presents the mapping from the parameter maps ( $W, F, R_2^*, f_{B_0}$ ) to the multi-echo images ( $\rho_m$ ), thus

$$\mathcal{B} : \mathbb{C}^{N^2 \times N_p} \mapsto \mathbb{C}^{N^2 \times E}. \quad (\text{A.6})$$

Here,  $N^2$  denotes the image size,  $N_p$  the number of parameter maps (4 in this case) and  $E$  the number of echoes. Therefore, its Jacobian matrix  $D\mathcal{B} \in \mathbb{C}^{N^2 \times E \times N_p}$ . Denote  $\mathcal{B}_m$  as the operator output corresponding to the  $m$ th TE, its corresponding Jacobian is

$$D\mathcal{B}_m = \left( \begin{array}{c} \frac{\partial \mathcal{B}_m}{\partial W} \\ \frac{\partial \mathcal{B}_m}{\partial F} \\ \frac{\partial \mathcal{B}_m}{\partial R_2^*} \\ \frac{\partial \mathcal{B}_m}{\partial f_{B_0}} \end{array} \right)^T = \left( \begin{array}{c} e^{-R_2^* \text{TE}_m} \cdot e^{i2\pi f_{B_0} \text{TE}_m} \\ z_m \cdot e^{-R_2^* \text{TE}_m} \cdot e^{i2\pi f_{B_0} \text{TE}_m} \\ F \cdot z_m \cdot ((-\text{TE}_m) e^{-R_2^* \text{TE}_m}) \cdot e^{i2\pi f_{B_0} \text{TE}_m} \\ (W + F \cdot z_m) \cdot e^{-R_2^* \text{TE}_m} \cdot (i2\pi \text{TE}_m) \cdot e^{i2\pi f_{B_0} \text{TE}_m} \end{array} \right)^T$$

The adjoint operator is then its complex conjugate transpose.

## ACKNOWLEDGMENT

Z. T. sincerely thanks Ms. Sarina Tepan for the organization of patients to evaluate the proposed method. Z. T. also thanks Drs. Jens Frahm, Li Feng, and Kai Tobias Block for various discussions. Z. T. and M. U. thank DFG for the research grant on TA 1473/2-1 and UE 189/4-1 (Project number: 427934942).

## REFERENCES

- [1] C. Caussy, S. B. Reeder, C. B. Sirlin, and R. Loomba, "Noninvasive, quantitative assessment of liver fat by MRI-PDFF as an endpoint in NASH trials," *Hepatology*, vol. 68, pp. 763–772, 2018.
- [2] H. H. Hu, R. T. Branca, D. Hernando, D. C. Karampinos, J. Machann, C. A. McKenzie, H. H. Wu, T. Yokoo, and S. S. Velan, "Magnetic resonance imaging of obesity and metabolic disorders: Summary from the 2019 ISMRM Workshop," *Magn. Reson. Med.*, vol. 83, pp. 1565–1576, 2020.
- [3] J. C. Wood, "Impact of iron assessment by MRI," *Hematology*, vol. 2011, pp. 443–450, 2011.
- [4] D. Hernando, Y. S. Levin, C. B. Sirlin, and S. B. Reeder, "Quantification of liver iron with MRI: State of the art and remaining challenge," *J. Magn. Reson. Imaging*, vol. 40, pp. 1003–1021, 2014.
- [5] W. T. Dixon, "Simple proton spectroscopic imaging," *Radiology*, vol. 153, pp. 189–194, 1984.
- [6] T. Armstrong, I. Dregely, A. Stemmer, F. Han, Y. Natsuaki, K. Sung, and H. H. Wu, "Free-breathing liver fat quantification using a multiecho 3D stack-of-radial technique," *Magn. Reson. Med.*, vol. 79, pp. 370–382, 2018.
- [7] X. Zhong, H. H. Hu, T. Armstrong, X. Li, Y.-H. Lee, T.-C. Tsao, M. D. Nickel, S. A. Kannengiesser, B. M. Dale, V. Deshpande, B. Kiefer, and H. H. Wu, "Free-breathing volumetric liver  $R_2^*$  and proton density fat fraction quantification in pediatric patients using stack-of-radial MRI With self-gating motion compensation," *J Magn. Reson. Imaging*, vol. 53, pp. 118–129, 2020.
- [8] X. Zhong, T. Armstrong, M. D. Nickel, S. A. R. Kannengiesser, L. Pan, B. M. Dale, V. Deshpande, B. Kiefer, and H. H. Wu, "Effect of respiratory motion on free-breathing 3D stack-of-radial liver  $R_2^*$  relaxometry and improved quantification accuracy using self-gating," *Magn. Reson. Med.*, vol. 83, pp. 1964–1978, 2020.
- [9] J. A. Fessler and B. P. Sutton, "Nonuniform fast Fourier transforms using min-max interpolation," *IEEE Trans. Signal Process.*, vol. 51, pp. 560–574, 2003.
- [10] H. Yu, C. A. McKenzie, A. Shimakawa, A. T. Vu, A. C. S. Brau, P. J. Beatty, A. R. Pineda, J. H. Brittain, and S. B. Reeder, "Multiecho reconstruction for simultaneous water-fat decomposition and  $T_2^*$  estimation," *J. Magn. Reson. Imaging*, vol. 26, pp. 1153–1161, 2007.
- [11] H. Yu, A. Shimakawa, C. A. McKenzie, E. Brodsky, J. H. Brittain, and S. B. Reeder, "Multiecho water-fat separation and simultaneous  $R_2^*$  estimation with multifrequency fat spectrum modeling," *Magn. Reson. Med.*, vol. 60, pp. 1122–1134, 2008.
- [12] V. V. Chebrolu, C. D. G. Hines, H. Yu, A. R. Pineda, A. Shimakawa, C. A. McKenzie, A. Samsonov, J. H. Brittain, and S. B. Reeder, "Independent estimation of  $T_2^*$  for water and fat for improved accuracy of fat quantification," *Magn. Reson. Med.*, vol. 63, pp. 849–857, 2010.
- [13] S. B. Reeder, A. R. Pineda, Z. Wen, A. Shimakawa, H. Yu, J. H. Brittain, G. E. Gold, C. H. Beaulieu, and N. J. Pelc, "Iterative decomposition of water and fat with echo asymmetry and least-squares estimation (IDEAL): Application with fast spin-echo imaging," *Magn. Reson. Med.*, vol. 54, pp. 636–644, 2005.
- [14] D. Hernando, P. Kellman, J. P. Haldar, and Z.-P. Liang, "Robust water/fat separation in the presence of large field inhomogeneities using a graph cut algorithm," *Magn. Reson. Med.*, vol. 63, pp. 79–90, 2010.
- [15] X. Zhong, M. D. Nickel, S. A. R. Kannengiesser, B. M. Dale, B. Kiefer, and M. R. Bashir, "Liver fat quantification using a multi-step adaptive fitting approach with multi-echo GRE imaging," *Magn. Reson. Med.*, vol. 72, pp. 1353–1365, 2014.
- [16] M. Schneider, T. Benkert, E. Solomon, D. Nickel, M. Fenchel, B. Kiefer, A. Maier, H. Chandarana, and K. T. Block, "Free-breathing fat and  $R_2^*$  quantification in the liver using a stack-of-stars multi-echo acquisition with respiratory-resolved model-based reconstruction," *Magn. Reson. Med.*, vol. 84, pp. 2592–2605, 2020.
- [17] K. T. Block, M. Uecker, and J. Frahm, "Model-based iterative reconstruction for radial fast spin-echo MRI," *IEEE Trans. Med. Imaging*, vol. 28, pp. 1759–1769, 2009.
- [18] J. A. Fessler, "Model-based image reconstruction for MRI," *IEEE Signal Processing Magazine*, vol. 27, pp. 81–89, 2010.
- [19] M. Doneva, P. Börnert, H. Eggers, A. Mertins, J. Pauly, and M. Lustig, "Compressed sensing for chemical shift-based water-fat separation," *Magn. Reson. Med.*, vol. 64, pp. 1749–1759, 2010.
- [20] N. Wang, T. Cao, F. Han, Y. Xie, X. Zhong, S. Ma, A. Kwan, Z. Fan, H. Han, X. Bi, M. Noureddin, V. Deshpande, A. G. Christodoulou, and D. Li, "Free-breathing multitasking multi-echo mri for whole-liver water-specific  $t_1$ , proton density fat fraction, and  $r_2^*$  quantification," *Magn. Reson. Med.*, vol. 87, pp. 120–137, 2022.

- [21] A. G. Christodoulou, J. L. Shaw, C. Nguyen, Q. Yang, Y. Xie, N. Wang, and D. Li, "Magnetic resonance multitasking for motion-resolved quantitative cardiovascular imaging," *Nat. Biomed. Eng.*, vol. 2, pp. 215–226, 2018.
- [22] J. Starekova, R. Zhao, T. J. Colgan, K. M. Johnson, J. L. Rehm, S. A. Wells, S. B. Reeder, and D. Hernando, "Improved free-breathing liver fat and iron quantification using a 2d chemical shift-encoded mri with flip angle modulation and motion-corrected averaging," *Eur. Radiol.*, vol. xx, pp. 1–12, 2022.
- [23] A. Buades, B. Coll, and J.-M. Morel, "A non-local algorithm for image denoising," in *Proc. IEEE Comput. Soc. Conf. Comput. Vis. Pattern Recognit.*, vol. 2, 2005, pp. 60–65.
- [24] B. P. Sutton, D. C. Noll, and J. A. Fessler, "Dynamic field map estimation using a spiral-in/spiral-out acquisition," *Magn. Reson. Med.*, vol. 51, pp. 1194–1204, 2004.
- [25] V. T. Olafsson, D. C. Noll, and J. A. Fessler, "Fast joint reconstruction of dynamic  $R_2^*$  and field maps in functional MRI," *IEEE Trans. Med. Imaging*, vol. 27, pp. 1177–1188, 2008.
- [26] A. K. Funai, J. A. Fessler, D. T. B. Yeo, V. T. Olafsson, and D. C. Noll, "Regularized field map estimation in MRI," *IEEE Trans. Med. Imaging*, vol. 27, pp. 1484–1494, 2008.
- [27] K. T. Block, H. Chandarana, S. Milla, M. Bruno, T. Mulholland, G. Fatterpekar, M. Hagiwara, R. Grimm, C. Geppert, B. Kiefer, and D. K. Sodickson, "Towards routine clinical use of radial stack-of-stars 3D gradient-echo sequences for reducing motion sensitivity," *J. Korean Soc. Magn. Reson. Med.*, vol. 18, pp. 87–106, 2014.
- [28] M. Uecker, T. Hohage, K. T. Block, and J. Frahm, "Image reconstruction by regularized nonlinear inversion – Joint estimation of coil sensitivities and image content," *Magn. Reson. Med.*, vol. 60, pp. 674–682, 2008.
- [29] S. Boyd, N. Parikh, E. Chu, B. Peleato, and J. Eckstein, "Distributed optimization and statistical learning via the alternating direction method of multipliers," *Foundations and Trends in Machine Learning*, vol. 3, pp. 1–122, 2010.
- [30] Z. Tan, D. Voit, J. M. Kollmeier, M. Uecker, and J. Frahm, "Dynamic water/fat separation and  $B_0$  inhomogeneity mapping – Joint estimation using undersampled triple-echo multi-spoke radial FLASH," *Magn. Reson. Med.*, vol. 82, pp. 1000–1011, 2019.
- [31] S. Winkelmann, T. Schaeffter, T. Koehler, H. Eggers, and O. Doessel, "An optimal radial profile based on the golden ratio for time-resolved MRI," *IEEE Trans. Med. Imaging*, vol. 26, pp. 68–76, 2007.
- [32] P. B. Roemer, W. A. Edelstein, C. E. Hayes, S. P. Souza, and O. M. Mueller, "The NMR phased array," *Magn. Reson. Med.*, vol. 16, pp. 192–225, 1990.
- [33] K. P. Pruessmann, M. Weiger, M. B. Scheidegger, and P. Boesiger, "SENSE: Sensitivity encoding for fast MRI," *Magn. Reson. Med.*, vol. 42, pp. 952–962, 1999.
- [34] M. A. Griswold, P. M. Jakob, R. M. Heidemann, M. Nittka, V. Jellus, J. Wang, B. Kiefer, and A. Haase, "Generalized autocalibrating partially parallel acquisitions (GRAPPA)," *Magn. Reson. Med.*, vol. 47, pp. 1202–1210, 2002.
- [35] S. B. Reeder, E. K. Bice, H. Yu, D. Hernando, and A. Pineda, "On the performance of  $T_2^*$  correction methods for quantification of hepatic fat content," *Magn. Reson. Med.*, vol. 67, pp. 389–404, 2012.
- [36] K. P. Pruessmann, M. Weiger, P. Börnert, and P. Boesiger, "Advances in sensitivity encoding with arbitrary k-space trajectories," *Magn. Reson. Med.*, vol. 46, pp. 638–651, 2001.
- [37] T. Zhang, J. M. Pauly, and I. R. Levesque, "Accelerated parameter mapping with a locally low rank constraint," *Magn. Reson. Med.*, vol. 73, pp. 655–661, 2015.
- [38] L. Feng, R. Grimm, K. T. Block, H. Chandarana, S. Kim, J. Xu, L. Axel, D. K. Sodickson, and R. Otazo, "Golden-angle radial sparse parallel MRI: Combination of compressed sensing, parallel imaging, and golden-angle radial sampling for fast and flexible dynamic volumetric MRI," *Magn. Reson. Med.*, vol. 72, pp. 707–717, 2014.
- [39] C. Hines, H. Yu, A. Shimakawa, C. A. McKenzie, J. H. Brittain, and S. B. Reeder, " $T_1$  independent,  $T_2^*$  corrected MRI with accurate spectral modeling for quantification of fat: Validation in a fat-water-SPIO phantom," *J Magn Reson Imaging*, vol. 30, pp. 1215–1222, 2009.
- [40] E. C. Bush, A. Gifford, C. L. Coolbaugh, T. F. Towse, B. M. Damon, and E. B. Welch, "Fat-water phantoms for magnetic resonance imaging validation: A flexible and scalable protocol," *J VIS EXP*, vol. 139, pp. 1–9, 2018.
- [41] M. Untenberger, Z. Tan, D. Voit, A. A. Joseph, V. Roeloffs, K.-D. Merboldt, S. Schätz, and J. Frahm, "Advances in real-time phase-contrast flow MRI using asymmetric radial gradient echoes," *Magn. Reson. Med.*, vol. 75, pp. 1901–1908, 2016.
- [42] M. Uecker, F. Ong, J. I. Tamir, D. Bahri, P. Virtue, J. Y. Cheng, T. Zhang, and M. Lustig, "Berkeley Advanced Reconstruction Toolbox," in *Proceedings of the 23th Annual Meeting of ISMRM, Toronto, CAN*, 2015, p. 2486.
- [43] F. Huang, S. Vijayakumar, Y. Li, S. Hertel, and G. R. Duensing, "A software channel compression technique for faster reconstruction with many channels," *Magn. Reson. Imaging*, vol. 26, pp. 133–141, 2008.
- [44] S. Rosenzweig, H. C. M. Holme, and M. Uecker, "Simple auto-calibrated gradient delay estimation from few spokes using Radial Intersections (RING)," *Magn. Reson. Med.*, vol. 81, pp. 1898–1906, 2019.
- [45] S. Rosenzweig, N. Scholand, H. C. M. Holme, and M. Uecker, "Cardiac and Respiratory Self-Gating in Radial MRI using an Adapted Singular Spectrum Analysis (SSA-FARY)," *IEEE Trans. Med. Imaging*, vol. 39, pp. 3029–3041, 2020.
- [46] C.-Y. Liu, C. A. McKenzie, H. Yu, J. H. Brittain, and S. B. Reeder, "Fat quantification with IDEAL gradient echo imaging: Correction of bias from T1 and noise," *Magn. Reson. Med.*, vol. 57, pp. 354–364, 2007.
- [47] G. Zhang, D. Allaire, and J. Cagan, "Taking the guess work out of the initial guess: A solution interval method for least-squares parameter estimation in nonlinear models," *ASME. J. Comput. Inf. Sci. Eng.*, vol. 21, 2021, 021011.
- [48] Z. Tan, T. Hohage, O. Kalentev, A. A. Joseph, X. Wang, D. Voit, K.-D. Merboldt, and J. Frahm, "An eigenvalue approach for the automatic scaling of unknowns in model-based reconstructions: Applications to real-time phase-contrast flow MRI," *NMR Biomed.*, vol. 30, p. e3835, 2017.
- [49] F. A. Breuer, M. Blaimer, R. M. Heidemann, M. F. Mueller, M. A. Griswold, and P. M. Jakob, "Controlled Aliasing in Parallel Imaging Results in Higher Acceleration (CAPIRINHA) for Multi-Slice Imaging," *Magn. Reson. Med.*, vol. 53, pp. 684–691, 2005.
- [50] E. Solomon, D. S. Rigie, T. Vahle, J. Paška, J. Bollenbeck, D. K. Sodickson, F. E. Boada, K. T. Block, and H. Chandarana, "Free-breathing radial imaging using a pilot-tone radiofrequency transmitter for detection of respiratory motion," *Magnetic Resonance in Medicine*, vol. 85, pp. 2672–2685, 2021.